IOP Publishing Nano Express 5 (2024) 015004 https://doi.org/10.1088/2632-959X/ad12d9

NANO EXPRESS

PAPER

SWCNT-Si photodetector with voltage-dependent active surface

Daniele Capista[1,*], **Luca Lozzi**[2], **Antonio Di Bartolomeo**[3,4], **Filippo Giubileo**[4], **Nadia Martucciello**[4] and **Maurizio Passacantando**[2,*]

[1] IHP–Leibniz Institut fuer innovative Mikroelektronik, 15236 Frankfurt (Oder), Germany
[2] Department of Physical and Chemical Science, University of L'Aquila, Via Vetoio, 67100 Coppito, L'Aquila, Italy
[3] Department of Physics 'E.R. Caianiello', University of Salerno, Fisciano 84084, Salerno, Italy
[4] CNR-SPIN Salerno, Fisciano 84084, Italy
[*] Authors to whom any correspondence should be addressed.

E-mail: capista@ihp-microelectronics.com **and** maurizio.passacantando@aquila.infn.it

Keywords: SWCNT, photodetectors, voltages, actives

OPEN ACCESS

RECEIVED
22 August 2023

REVISED
3 November 2023

ACCEPTED FOR PUBLICATION
6 December 2023

PUBLISHED
22 December 2023

Abstract

New works on Carbon Nanotubes-Silicon MIS heterostructures showed that the presence of thickness inhomogeneities in the insulating layer across the device can be exploited to increase their functionalities. In this work, we report the fabrication and characterization of a device consisting of a Single-Walled Carbon Nanotube (SWCNT) film onto an *n*-type silicon substrate where the nitride interlayer between the nanotubes and the silicon has been intentionally etched to obtain different thicknesses. Three different silicon nitride thicknesses allow the formation of three regions, inside the same device, each with different photocurrents and responsivity behaviors. We show that by selecting specific biases, the photoresponse of the regions can be switched on and off. This peculiar behavior allows the device to be used as a photodetector with a voltage-dependent active surface. Scanning photo response imaging of the device surface, performed at different biases, highlights this behavior.

1. Introduction

Photodetectors are our society's most used technological devices, with applications in day-life, medical, military, and research fields [1–4]. They can be realized using different materials or structures [5–9] but the oldest and best-understood photonic devices, with commercial products that can operate in the range from 300 to 900 nm, are the silicon photodetectors [10]. Despite their advanced technology, different intrinsic problems, such for example, the low absorption in the ultraviolet (UV) and infrared (IR) regions, still limit their possible applications. In the last years, conventional silicon photodetectors have been combined with low-dimensional materials not only to improve their performances but also to add further functionalities [11–14]. Among these materials, carbon nanotubes (CNT), with their outstanding electrical and mechanical properties, are often used to realize improved photodetectors [15–21]. Due to their high electrical conductivity and optical transparency, CNTs are used as antireflective and conductive electrodes for photo charge collection inside photodetectors based on the CNT/Si heterojunction [22–25]. Such heterojunction often includes an insulating layer between the two materials that results in an increase of the Schottky barrier height and a reduction of the leakage current of the device. The insulating layer allows also a more complex charge transport across the junction, where tunneling transport is added to thermionic transport [26–30]. The work of Pelella *et al* [20] showed that the presence of inhomogeneities in the nitride layer (in that case induced by the electrical stress) could be exploited to add more functionalities to the device.

Following that observation, we intentionally modified the silicon nitride (Si_3N_4) thickness on top of the Si substrate to obtain wide regions with different nitride layers. The idea of this study was to realize a single device with different silicon nitride thicknesses and characterize its properties. Owing to the different Si_3N_4 thicknesses, the active area of the device can be tuned by the applied bias, which is an important new functionality. Having three different devices on different substrates would not enable the bias control of the device's active area. Indeed, the presence of regions of different silicon nitride allowed the formation of different

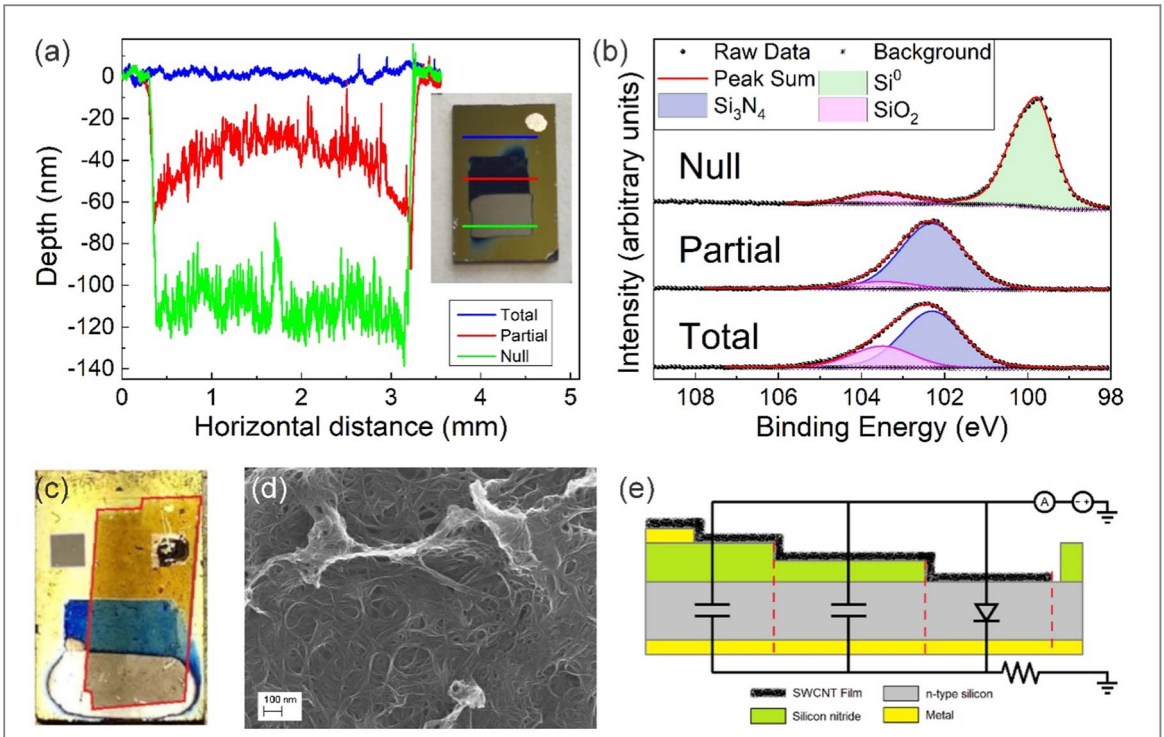

Figure 1. (a) Depth profile across the lines in the three regions of the substrate after the etching of the Si_3N_4 layer by hydrofluoric acid. (b) Si 2p core level spectra in the three regions. (c) Optical image of the device. In red is highlighted the border of the SWCNT film. The two rectangles (grey and dark) in the upper part of the chip are the Pt-Ta pads. (d) High-resolution SEM images of a SWCNT film deposited with the transfer printing method. (e) Schematic representation of the device with the different nitride thicknesses.

junctions coexisting in the same device and with a different photocurrent behavior associated with each one of them. Moreover, we showed that by selecting specific biases, the responsivity values of each region could be associated with an 'activated' or 'deactivated' state. This feature suggested that the device could be used as a photodetector in which the active area could be changed with the applied bias. Using scanning photo response imaging of the device surface we provide a visual demonstration of how the device's active surface changes as a function of the applied bias. Following the demonstration of the general concept of a photodetector with a bias-tuneable active area, the scaling down of the device dimensions will allow its optimization in terms of power consumption, photoresponse, and response time.

2. Experimental details

The device was realized starting from a silicon substrate composed of a 500 μm n-type silicon wafer (resistivity 1–5 Ω cm, doping 10^{15} cm^{-3}) with the top surface covered by a Si_3N_4 layer of 140 nm nominal thickness. The substrate presented two metallic pads of 1 mm^2 area (50 nm Pt over 10 nm Ta) on the top surface and a metallic layer (same structure as the pads) on the bottom surface as the back contact. The thickness of the nitride layer was tuned using a wet etching process. The substrate was completely covered by a Kapton tape mask to protect the metallic contacts and avoid unwanted etching, a small window was made on the tape to expose only a selected portion of the surface. After that, the substrate was placed in a plastic vial containing a room-temperature 5% hydrofluoric acid (HF) water solution to start the etching process [31]. Once reached the desired thickness the substrate was removed from the HF and rinsed with distilled water. We repeated the etching in two adjacent regions of the substrate. In this way, we obtained three different thicknesses across the substrate surface: one with the 'total' nitride, one with a 'partial' and one with a 'null' nitride layer (in the text we will refer to these regions as 'nitride' regions, even if the third region as no nitride). The depth profiles across the three regions are reported in figure 1(a), revealing that that the total nitride layer thickness is 120 nm while the intermediate region has an average thickness of 70 nm.

X-ray photoemission spectroscopy (XPS) was used to analyze the chemical composition of the surfaces, especially to confirm the complete removal of nitride in the third region. Figure 1(b) reports the deconvoluted XPS spectra of the Si 2p core level acquired in the three regions. The spectra were fitted by the sum of three signals: the Si^0 (99.7 eV, characterized by a spin–orbit splitting of 0.6 eV), the Si_3N_4 signal (102.3 eV), and the silicon oxide (103.4 eV) [32, 33]. The unetched surface presents a strong signal due to the Si-N bonds, with a

non-negligible signal due to silicon oxide. The partially etched region shows a spectrum like the unetched one but with a reduced oxide signal. The thickness of the nitride in the partial region is still too high to allow the observation of the signal coming from the silicon wafer. Finally, the completely etched surface shows a strong signal at lower binding energies attributed to the pure silicon. The small oxide signal indicates the formation of native oxide on the silicon surface after the etching process.

Following the characterization of the substrate surface, a single-walled carbon nanotube film was deposited on the substrate surface using the transfer printing method [19, 34]. To facilitate the electric contact, the SWCNT film was deposited onto one of the metallic pads and made large enough to cover all three surface regions. Figure 1(c) shows an optical image of the device after the deposition process. The three regions are easily recognizable by their colors, in the vertical direction: the full nitride layer has a yellow-green color, the partially etched is blue while the region without nitride is grey. The morphology of the film was analyzed with a scanning electron microscope (SEM) using an accelerating voltage of 5 kV. Figure 1(d) shows that the film is composed of randomly oriented nanotubes that form an intricated three-dimensional structure above the device surface.

We measured the current–voltage characteristics of the device using the top Pt-Ta pad covered by the CNT film and the back contact of the substrate respectively as anode and cathode. The electrical behavior of the device was tested both in the dark and under a 650 nm laser light ($P = 100\ \mu$W) focused on each of the three nitride regions. Due to the absence of the nitride layer in the 'Null' region, a metal-semiconductor junction (MS diode) is directly formed between the nanotubes and the exposed silicon. Differently from Pelella's work, the device did not need to undergo heavy electrical stresses to become electrically conductive. Therefore, the nitride layers in the other regions remain undamaged and it is possible to consider them as MIS capacitors. The entire photodetector can be modeled as the parallel of two MIS capacitors with different insulator thicknesses and an MS diode (figure 1(e)).

All the electrical measurements, from the IV characteristic to the time response behavior of the device, were performed using a Keithley 236 Source-Measure unit directly connected to the device by BNC cables.

3. Results

3.1. Photocurrent behaviors

Compared to similar SWCNT-Si devices [19, 20], the 'Dark' I-V curve reported in figure 2(a) shows a low rectifying behavior (the on–off ratio calculated at $V = \pm 10$ V is only 2.3). This is due to the presence of the large SWCNT-Si junction ('null' region) that yields a high reverse current [26, 35].

Despite the poor rectification caused by the SWCNT-Si diode, it is possible to see that the device exhibits completely different photocurrent behaviors when a small light spot (diameter less than 1 mm) is focused on the different regions (figure 2(a)). When the spot is located above the 'Total' nitride layer (blue curve), the current follows the 'Dark' till the voltage of −5 V. After that value the current increases, indicating the production of a photocurrent: $I_{photo}(V) = I_{light}(V) - I_{dark}(V)$.

If the light spot is moved on the 'Partial' region, the voltage after which the photocurrent becomes appreciable gets closer to zero. The linear behavior of these two photocurrents in the Fowler–Nordheim (F-N) plot in figure 2(b) demonstrates that the photocurrent is due to charges tunneling through the triangular barrier in the MIS capacitors [19, 20, 36]. The F-N plot also highlights that the charges begin to tunnel through the nitride layer at different biases, depending on the insulator thickness. We observe a turn-on voltage of $V^{Turn-on} = -1.5V$ for the 'Partial' capacitor and $V^{Turn-on} = -5V$ for the 'Total' capacitor.

Finally, when the light is focused above the MS diode the detector shows also photovoltaic properties. The I-V curve in figure 2(c) shows that a 650 nm laser light at $P_{light} = 100\ \mu$W focused on the MS diode produces an open-circuit voltage $V_{oc} = V(I = 0) = 0.27$ V and a short-circuit current $I_{sc} = I(V = 0) = 0.72\ \mu$A, resulting in a current responsivity ($R_I = I_{sc}/P_{light}$) of 720 μA W^{-1}.

Figure 2(d) reports the photocurrent collected over a larger voltage range, highlighting the presence of a maximum in the photocurrent that was not observable in figure 2(a). The light impinging on the substrate generates electron–hole pairs inside silicon, that get separated by the electric field, collected by the nanotubes, and originate the photocurrent. If the photo-charges are generated inside an MIS capacitor, the photocurrent does not vary from the dark one until the turn-on voltage for F-N tunneling is reached. With the increasing reverse bias, more photo-charges are collected at the contacts, resulting in an increase of the current. When the light is directed on the MS diode instead the charges can be separated by the built-in potential so there is no need to reach a turn-on voltage to see a photocurrent. The currents grow with the reverse bias until they reach a plateau caused by the series resistance. From figure 2(d) is also possible to notice that the different photocurrent behaviors allow the selection of specific voltage values in which one or both the MIS capacitors had a small response.

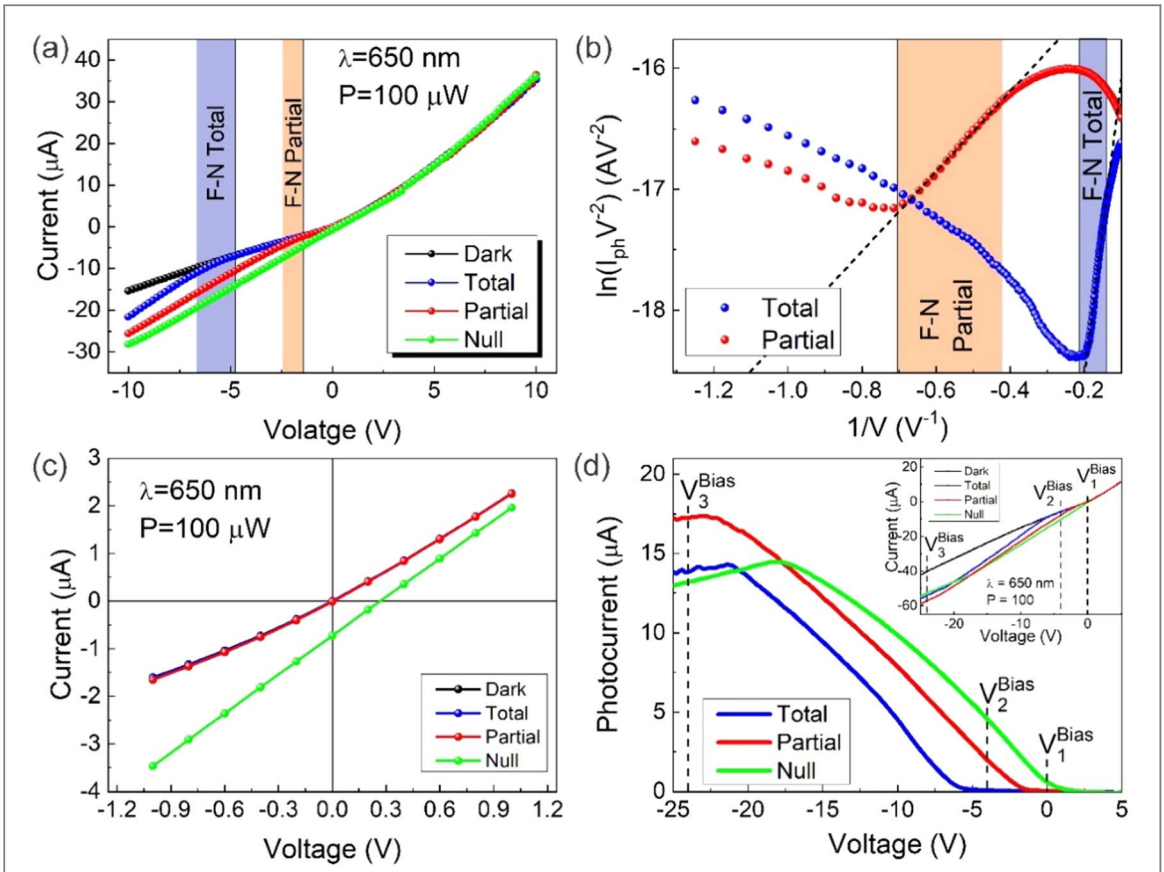

Figure 2. (a) I-V characteristic of the device in dark and under illumination with the spot focused on the different regions of the device with 'Total', 'Partial', and 'Null' nitride thickness. (b) Fowler–Nordheim plot of the photocurrents measured for the total and partial MIS capacitor. The dashed line highlights the linear behavior in the F-N region. (c) Detail of the currents around 0 V that shows an open circuit voltage near 300 mV and a short circuit current about 0.7 μA. (d) Photocurrent and I-V characteristic (Inset) in a wider voltage range. In both pictures, the biases used for the linear characterization of the device responsivity behavior are highlighted.

To obtain better information about the responsivity and the linearity response of the device we measured the I-V characteristics of each region under irradiation by a 650 nm laser with different light powers. The photocurrents produced by the different light powers were calculated for the three biases reported in figure 2(d) to highlight the presence of linear behaviors in the different working conditions. The first bias was set to $V_1^{Bias} = 0$ V to characterize the photovoltaic mode of the device. The second bias at $V_2^{Bias} = -4$ V was chosen to highlight the response of the device in a region where only the MS diode and the partial MIS capacitor are active and finally, the third bias was set at $V_3^{Bias} = -24$ V to characterize the response of the device in the plateau region.

Figure 3 shows the values of the photocurrent at different biases as a function of the impinging light power for the three regions of the device. To highlight the presence of small photocurrents we reported the values in two graphs, one for currents in the order of microampere and one for that in the nanoampere. When the light is focused on the unetched nitride layer (figure 3(a)), the photocurrents reach values in the order of microampere only when strong reverse bias is applied to the device, while with lower bias voltages the photocurrents remain in the order of nanoampere. The photocurrents measured at high reverse bias and the one at zero bias show linear behavior over the explored power range, while at low reverse bias, the behavior is not well defined.

When the light is focused on the partially etched nitride (figure 3(b)), the photocurrents at -4 V are greatly enhanced. Now is possible to observe a microampere current flowing through the device, but there is still no complete linearity: at lower powers, the photocurrent values follow a trend that is comparable to that of the plateau region, but a saturation occurs at higher powers. In the cases of high reverse bias and with no external bias the values of photocurrents follow a linear behavior for all the impinging powers.

Finally, when the light is focused on the MS diode (figure 3(c)), the full linear behavior is preserved only when the current is measured at the plateau, while in the other cases, the photocurrents have an initial linear behavior that ends in saturation. Now also the photocurrent measured without bias can reach values close to the microampere.

We used different approaches to calculate the average responsivity depending on the behavior of the current with respect to the impinging light power. When the structures show a linear behavior, the 'average' responsivity

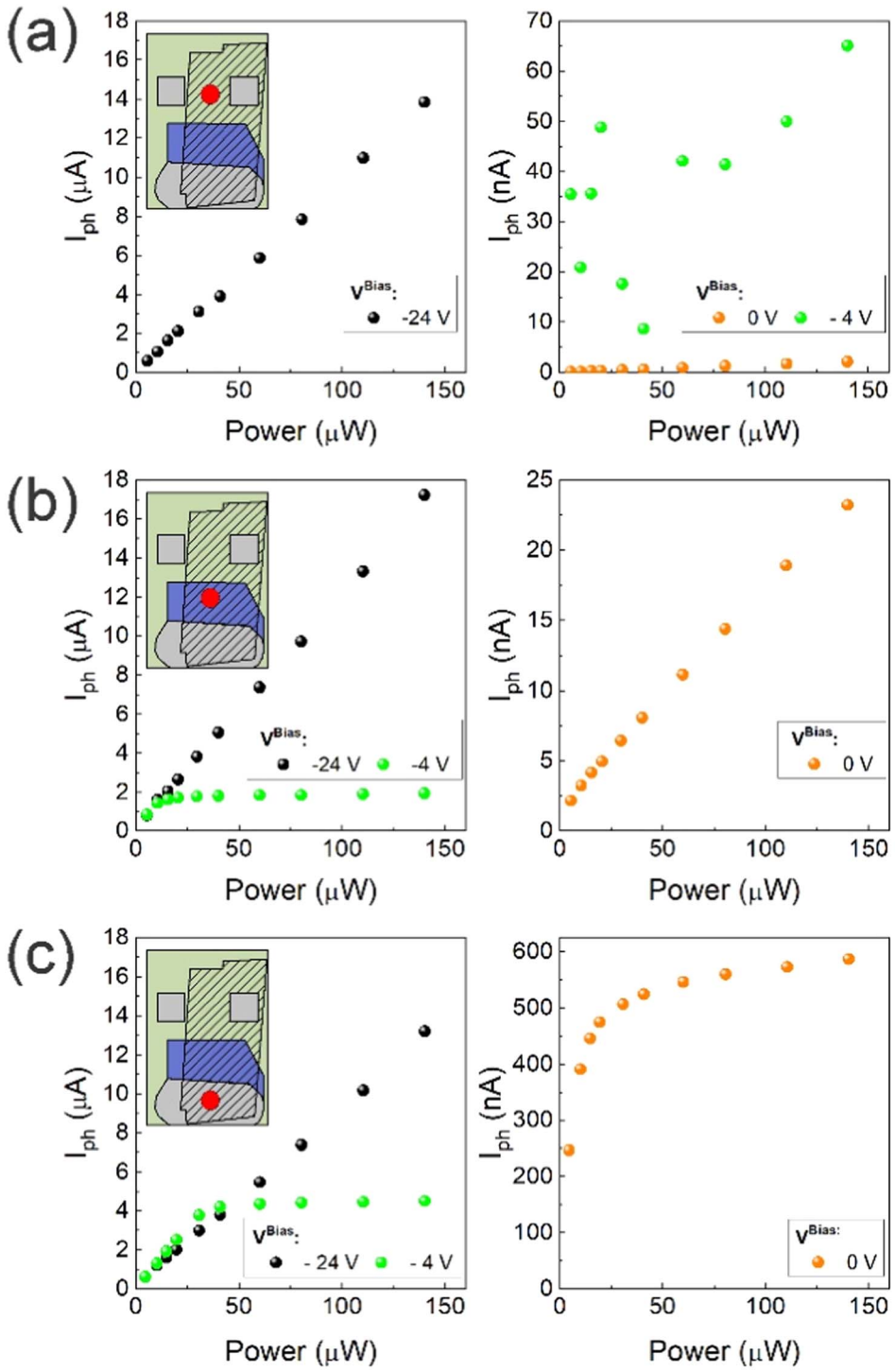

Figure 3. Photocurrent at different biases for (a) MIS capacitor with total nitride layer, (b) MIS capacitor with partially etched nitride, and (c) MS diode.

is evaluated from the slope of the linear fit of all the data reported in figure 3. When saturation occurs, since the photocurrent does not increase with the impinging light power, the 'single' value of responsivity (calculated as the photocurrent value divided by the impinging power) shows a decreasing trend with the increasing power. In these cases, the maximum value of responsivity is evaluated from a linear fit restricted to the region before the saturation. The responsivity of the different structures (and the associated error obtained from the fit) are summarized in table 1. The table shows that there are mainly two different regimes: one with a low (orange entries in table 1) and one with high responsivity (green entries in table 1). By considering a region 'activated' only when the responsivity has a high value ($\sim 10^{-2}$ A W^{-1}) it is possible to notice that depending on the selected voltage bias (0, −4 or −24 V), a different number of regions can be activated (one, two or three respectively). For

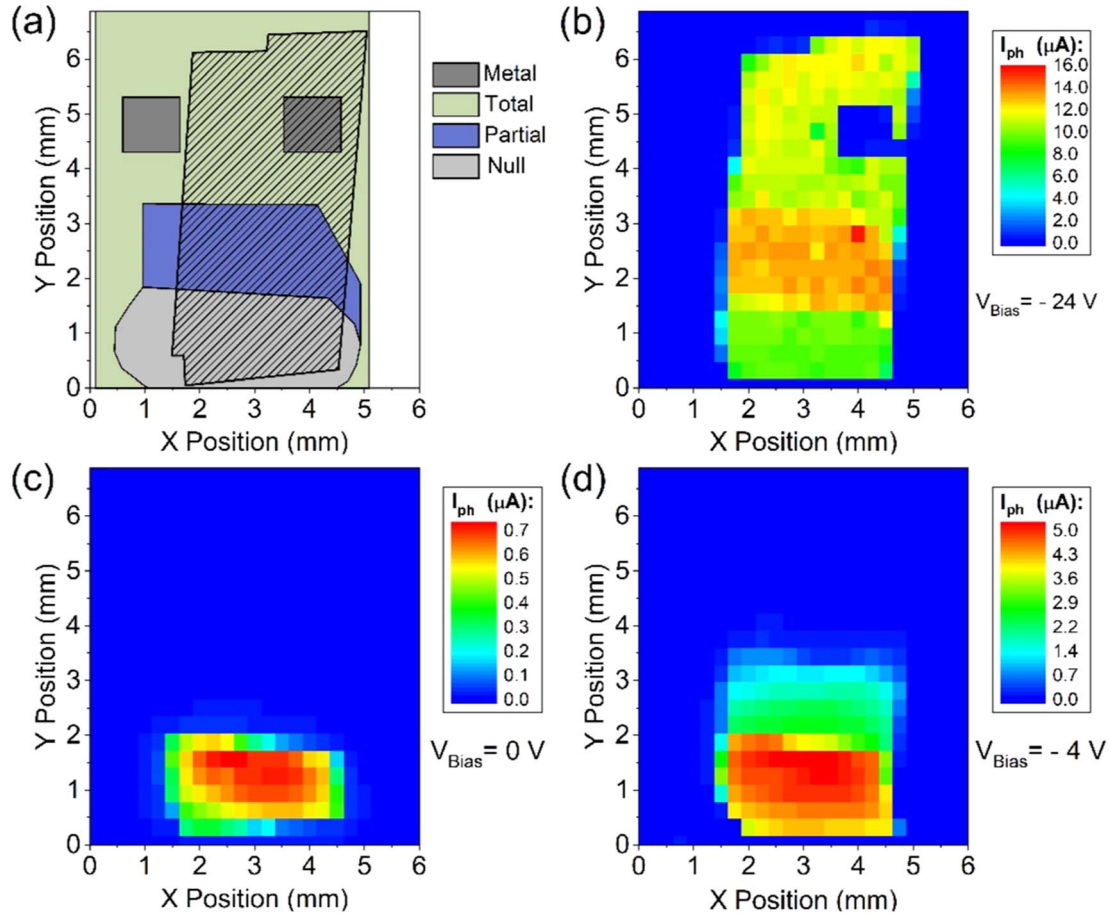

Figure 4. (a) In-scale schematic top view of the device. Extracted photocurrent maps at −24 V (b), 0 V (c), and −4 V (d).

Table 1. Responsivity of the device regions at the different biases. The style of each entry highlights if the structure is active (**bold**) or not active (*italic*) for that bias value.

Spot position	Responsivity (A/W)		
	V = 0 V	V = − 4 V	V = −24 V
MIS Capacitor (Total)	*(1.48 ± 0.03) 10^{-5}*	*(24.1 ± 9.9) 10^{-5}*	**(9.9 ± 0.1) 10^{-2}**
MIS Capacitor (Partial)	*(15.6 ± 0.1) 10^{-5}*	**(7.8 ± 2.4) 10^{-2}**	**(12.1 ± 0.1) 10^{-2}**
MS Diode	**(1.5 ± 0.3) 10^{-2}**	**(12.1 ± 0.2) 10^{-2}**	**(9.1 ± 0.1) 10^{-2}**

example, the voltage of −24 V enables the photocurrent production from all three structures (with a similar response), while a reverse bias of −4 V, strongly suppresses the photocurrent from the 'Total' capacitor.

3.2. Photocurrent mapping

To highlight this behavior, we acquired several photocurrent maps of the device using the scanning photocurrent imaging techniques [20, 37]. To help the description of the maps, figure 4(a) reports an in-scale schematic of the device shown in figure 1(c). The map acquired at $V = -24$ V (i.e., in the plateau region of the photocurrents) shows that all the area covered by the nanotube film is responding to the incoming light, while the rest of the device does not produce any photocurrent. The region below the pad is not responding since the metal layer reflects completely the radiation and no photo charges can be generated inside the underlying silicon substrate. A slightly higher photocurrent can be measured in the partially etched region with respect to the unetched one, where the thicker nitride layer suppresses the charge collection and simultaneously absorbs the incident photons. Independently on its thickness, the presence of the nitride layer positively affects the device response; indeed, the photocurrents measured on the MIS capacitors are always higher than that measured on the MS diode [30, 38–43].

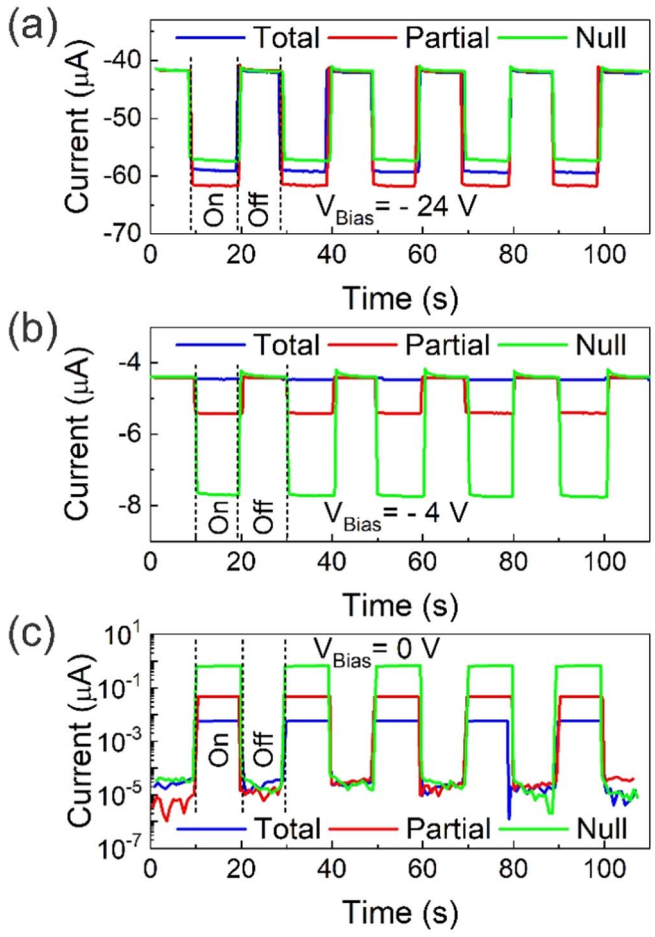

Figure 5. Time response of the device in the plateau region (a), at an intermediate voltage (b), and at zero voltage (c). The last graph is reported in a semi-log scale to highlight the different orders of magnitude of the photo response.

We showed that by varying the voltage bias, the photosensitive area of the device can be tuned accordingly to the thickness of the nitride layer. Without bias (figure 4(c)), only the MS diode, which can work in photovoltaic mode, is active while when the reverse bias is increased to –4 V, (a voltage slightly higher than the turn-on voltage of the 'Partial' MIS capacitor and at the same time smaller than that of the 'Total' MIS capacitor) also the Partial MIS capacitor starts to respond.

To conclude the analysis the time response of the device has been tested with repeated on/off cycles of a 650 nm laser light at 200 μW power. The responses acquired for all the regions at different bias is reported in figure 5. In all cases, the time response is faster than the 500 ms limit set by the experimental setup and stable for all the observed time. Figure 5(c) shows the current on a semi-log scale acquired at 0 V, highlighting the magnitude of the currents produced in the photovoltaic mode in the three regions.

4. Conclusions

We have fabricated and studied a photodetector made of a heterojunction between SWCNTs and a silicon substrate. The substrate, initially composed of an *n*-doped silicon wafer covered by a thick Si_3N_4 layer, was wet-etched to obtain a three-zone device with the total, partial, and 'absent' thickness of the nitride.

The I-V characteristics of the device show diode-like behavior with low rectification, mostly due to the large contact area of the junction with the exposed silicon. The device was modeled as the parallel of two MIS capacitors and an MS diode. The presence of these structures results in a photocurrent that strongly depends on the illuminated region. While the MS region could produce a photocurrent even with no reverse bias, the two MIS capacitors, were able to produce a photocurrent only after a voltage threshold, required to enable Fowler–Nordheim tunneling through the insulating layer ('−5 V for the 'Total' region and −1.5 V for the 'Partial'). By selecting appropriate values of reverse bias, we were able to obtain responsivity with values belonging to only two ranges. Due to the large difference between these ranges, it was possible to associate one as the activated' and 'deactivated' state of the structures. Depending on the bias voltage, the response from one or both MIS

capacitors could be turned off. This allowed us to vary the active surface of the device by changing the voltage bias.

Data availability statement

The data cannot be made publicly available upon publication because they are not available in a format that is sufficiently accessible or reusable by other researchers. The data that support the findings of this study are available upon reasonable request from the authors.

Conflict of interest

The authors have no conflicts to disclose.

Author contributions

Daniele Capista: Data Curation (equal); Formal analysis (equal); Investigation (equal); Writing—original draft (equal); Writing—review & editing (equal). **Luca Lozzi:** Investigation (equal); Resources (equal); Validation (equal). **Antonio Di Bartolomeo:** Formal analysis (equal); Supervision (equal); Validation (equal); Writing—review & editing (equal). **Filippo Giubileo:** Methodology (equal); Validation (equal); Writing—review & editing (equal). **Nadia Martucciello:** Methodology (equal); Visualization (equal). **Maurizio Passacantando:** Supervision (equal); Resources (equal); Validation (equal); Writing—review & editing (equal).

ORCID iDs

Antonio Di Bartolomeo https://orcid.org/0000-0002-3629-726X
Filippo Giubileo https://orcid.org/0000-0003-2233-3810
Maurizio Passacantando https://orcid.org/0000-0002-3680-5295

References

[1] Mueller T, Xia F and Avouris P 2010 Graphene photodetectors for high-speed optical communications *Nat. Photonics* **4** 297–301
[2] Lahiri B B, Bagavathiappan S, Jayakumar T and Philip J 2012 Medical applications of infrared thermography: a review *Infrared Phys. Technol.* **55** 221–35
[3] Ryzhii V, Otsuji T, Karasik V E, Ryzhii M, Leiman V G, Mitin V and Shur M S 2018 Comparison of intersubband quantum-well and interband graphene-layer infrared photodetectors *IEEE J. Quantum Electron.* **54** 1–8
[4] Agostinelli T, Campoy-Quiles M, Blakesley J C, Speller R, Bradley D D C and Nelson J 2008 A polymer/fullerene based photodetector with extremely low dark current for x-ray medical imaging applications *Appl. Phys. Lett.* **93** 203305
[5] Sarcan F, Nutku F, Nordin M S, Vickers A J and Erol A 2018 A study on the voltage-dependent response of a GaInNAs-based pin photodetector with a quasi-cavity *Semicond. Sci. Technol.* **33** 114006
[6] Doğan Ü, Sarcan F, Koç K K, Kuruoğlu F and Erol A 2022 Effects of annealing temperature on a ZnO thin film-based ultraviolet photodetector *Phys. Scr.* **97** 015803
[7] Sarcan F, Orchard S, Kuerbanjiang B, Skeparovski A, Lazarov V K and Erol A 2020 Ultraviolet photodetector based on Mg0.67Ni0.33O thin film on SrTiO3 *Physica Status Solidi RRL* **14** 2000175
[8] Balkan N, Erol A, Sarcan F, Al-Ghuraibawi L F F and Nordin M S 2015 Dilute nitride resonant cavity enhanced photodetector with internal gain for the $\lambda \sim 1.3$ μm optical communications window *Superlattices Microstruct.* **86** 467–71
[9] Sarcan F, Doğan U, Althumali A, Vasili H B, Lari L, Kerrigan A, Kuruoğlu F, Lazarov V K and Erol A 2023 A novel NiO-based p-i-n ultraviolet photodiode *J. Alloys Compd.* **934** 167806
[10] Jalali B and Fathpour S 2006 Silicon Photonics *J. Lightwave Technol.* **24** 4600–15
[11] Diao J, Srivastava D and Menon M 2008 Molecular dynamics simulations of carbon nanotube/silicon interfacial thermal conductance *J. Chem. Phys.* **128** 164708
[12] Aramo C, Ambrosio A, Ambrosio M, Battiston R, Castrucci P, Cilmo M, De Crescenzi M, Fiandrini E, Guarino F and Grossi V 2013 Development of new photon detection device for Cherenkov and fluorescence radiation *EPJ Web of Conferences* **53** (EDP Sciences) 8014
[13] Li X, Mariano M, McMillon-Brown L, Huang J, Sfeir M Y, Reed M A, Jung Y and Taylor A D 2017 Charge transfer from carbon nanotubes to silicon in flexible carbon nanotube/silicon solar cells *Small* **13** 1702387
[14] Li X, Lv Z and Zhu H 2015 Carbon/silicon heterojunction solar cells: state of the art and prospects *Adv. Mater.* **27** 6549–74
[15] Poudel Y R and Li W 2018 Synthesis, properties, and applications of carbon nanotubes filled with foreign materials: a review *Mater. Today Phys.* **7** 7–34
[16] Lamura G *et al* 2007 High-crystalline single- and double-walled carbon nanotube mats grown by chemical vapor deposition *J. Phys. Chem.* C **111** 15154–9
[17] Bartolomeo A D, Rinzan M, Boyd A K, Yang Y, Guadagno L, Giubileo F and Barbara P 2010 Electrical properties and memory effects of field-effect transistors from networks of single-and double-walled carbon nanotubes *Nanotechnology* **21** 115204
[18] Belin T and Epron F 2005 Characterization methods of carbon nanotubes: a review *Materials Science and Engineering:* B **119** 105–18

[19] Capista D, Passacantando M, Lozzi L, Faella E, Giubileo F and Di Bartolomeo A 2022 Easy Fabrication of Performant SWCNT-Si Photodetector *Electronics (Basel)* **11** 271
[20] Pelella A, Capista D, Passacantando M, Faella E, Grillo A, Giubileo F, Martucciello N and Di Bartolomeo A A 2023 Self-powered CNT–Si photodetector with tuneable photocurrent *Adv. Electron. Mater.* **9** 2200919
[21] Camilli L, Capista D, Eramo P, D'Archivio A A, Maggi M A, Lazzarini A, Crucianelli M and Passacantando M 2022 Synthesis of hydrophilic carbon nanotube sponge via post-growth thermal treatment *Nanotechnology* **33** 245707
[22] Del Gobbo S, Castrucci P, Scarselli M, Camilli L, De Crescenzi M, Mariucci L, Valletta A, Minotti A and Fortunato G 2011 Carbon nanotube semitransparent electrodes for amorphous silicon based photovoltaic devices *Appl. Phys. Lett.* **98** 183113
[23] Yu L, Shearer C and Shapter J 2016 Recent development of carbon nanotube transparent conductive films *Chem. Rev.* **116** 13413–53
[24] Tune D D and Shapter J G 2013 Effect of nanotube film thickness on the performance of nanotube-silicon hybrid solar cells *Nanomaterials* **3** 655–73
[25] Wu Z *et al* 2004 Transparent, conductive carbon nanotube films *Science (1979)* **305** 1273–6
[26] Al-Ahmadi N A 2020 Metal oxide semiconductor-based schottky diodes: a review of recent advances *Mater. Res. Express* **7** 32001
[27] Giubileo F, Iemmo L, Luongo G, Martucciello N, Raimondo M, Guadagno L, Passacantando M, Lafdi K and Di Bartolomeo A 2017 Transport and field emission properties of buckypapers obtained from aligned carbon nanotubes *J. Mater. Sci.* **52** 6459–68
[28] Pelella A, Grillo A, Faella E, Luongo G, Askari M B and Di Bartolomeo A 2021 Graphene–silicon device for visible and infrared photodetection *ACS Appl. Mater. Interfaces* **13** 47895–903
[29] Hu X, Hou P, Liu C and Cheng H 2019 Carbon nanotube/silicon heterojunctions for photovoltaic applications *Nano Materials Science* **1** 156–72
[30] Jia Y, Cao A, Kang F, Li P, Gui X, Zhang L, Shi E, Wei J, Wang K and Zhu H 2012 Strong and reversible modulation of carbon nanotube–silicon heterojunction solar cells by an interfacial oxide layer *Phys. Chem. Chem. Phys.* **14** 8391–6
[31] Knotter D M and Denteneer T J J D 2001 Etching mechanism of silicon nitride in HF-based solutions *J. Electrochem. Soc.* **148** F43
[32] Alfonsetti R, De Simone G, Lozzi L, Passacantando M, Picozzi P and Santucci S 1994 SiOx surface stoichiometry by XPS: a comparison of various methods *Surf. Interface Anal.* **22** 89–92
[33] Lozzi L, Passacantando M, Picozzi P, Santucci S, Tomassi G, Alfonsetti R and Borghesi A 1994 Surface stoichiometry determination of SiOxNy thin films by means of XPS *Surf. Interface Anal.* **22** 190–2
[34] De Nicola F, Castrucci P, Scarselli M, Nanni F, Cacciotti I and De Crescenzi M 2015 Multi-Fractal Hierarchy of Single-Walled Carbon Nanotube Hydrophobic Coatings *Scientific Reports* **5** 8583
[35] Shetty A, Roul B, Mukundan S, Mohan L, Chandan G, Vinoy K J and Krupanidhi S B 2015 Temperature dependent electrical characterisation of Pt/HfO2/n-GaN metal-insulator-semiconductor (MIS) Schottky diodes *AIP Adv.* **5** 97103
[36] Di Bartolomeo A, Giubileo F, Grillo A, Luongo G, Iemmo L, Urban F, Lozzi L, Capista D, Nardone M and Passacantando M 2019 Bias tunable photocurrent in metal-insulator-semiconductor heterostructures with photoresponse enhanced by carbon nanotubes *Nanomaterials* **9** 1598
[37] Capista D, Lozzi L, Pelella A, Di Bartolomeo A, Giubileo F and Passacantando M 2023 Spatially resolved photo-response of a carbon nanotube/si photodetector *Nanomaterials* **13** 650
[38] Ouyang W, Teng F, He J and Fang X 2019 Enhancing the photoelectric performance of photodetectors based on metal oxide semiconductors by charge-carrier engineering *Adv. Funct. Mater.* **29** 1807672
[39] Luongo G, Di Bartolomeo A, Giubileo F, Chavarin C A and Wenger C 2018 Electronic properties of graphene/p-silicon Schottky junction *J. Phys. D: Appl. Phys.* **51** 255305
[40] Riazimehr S, Kataria S, Gonzalez-Medina J M, Wagner S, Shaygan M, Suckow S, Ruiz F G, Engström O, Godoy A and Lemme M C 2018 High responsivity and quantum efficiency of graphene/silicon photodiodes achieved by interdigitating Schottky and gated regions *ACS Photonics* **6** 107–15
[41] Riazimehr S, Belete M, Kataria S, Engström O and Lemme M C 2020 Capacitance–voltage (C–V) characterization of graphene–silicon heterojunction photodiodes *Adv. Opt. Mater.* **8** 2000169
[42] Riazimehr S, Kataria S, Bornemann R, Haring Bolívar P, Ruiz F J G, Engström O, Godoy A and Lemme M C 2017 High photocurrent in gated graphene–silicon hybrid photodiodes *ACS Photonics* **4** 1506–14
[43] Di Bartolomeo A, Luongo G, Giubileo F, Funicello N, Niu G, Schroeder T, Lisker M and Lupina G 2017 Hybrid graphene/silicon Schottky photodiode with intrinsic gating effect *2D Mater.* **4** 25075